Surface & Coatings Technology 450 (2022) 129002

Contents lists available at ScienceDirect

Surface & Coatings Technology

journal homepage: www.elsevier.com/locate/surfcoat

Influence of HiPIMS pulse widths on the deposition behaviour and properties of CuAgZr compositionally graded films

L. Lapeyre [a,*], K. Wieczerzak [b], C. Hain [a,b], J. Metzger [c], A. Sharma [b], A. Bensaoula [a,c], J. Michler [b], T. Nelis [a,b]

[a] Bern University of Applied Sciences, Institute for Applied Laser, Photonics and Surface Technologies ALPS, Quellgasse 21, 2502 Biel/Bienne, Switzerland
[b] Empa, Swiss Federal Laboratories for Materials Science and Technology, Laboratory for Mechanics of Materials and Nanostructures, Feuerwerkerstrasse 39, 3602 Thun, Switzerland
[c] Tofwerk AG, Schorenstrasse 39, 3645 Thun, Switzerland

ARTICLE INFO

Keywords:
CuAgZr system
Metallic glasses
HiPIMS
Plasma diagnostics
Material characterisation

ABSTRACT

In this work, the influence of different pulse widths (25, 50 and 100 μs) during high power impulse magnetron sputtering (HiPIMS) of copper, silver and zirconium was investigated in terms of plasma properties and properties of combinatorial composition gradient CuAgZr film libraries. In situ plasma diagnostics via optical emission spectroscopy (OES), time-of-flight mass spectrometry (TOFMS), and modified quartz crystal microbalance (m-QCM), followed by film ex situ X-ray diffraction (XRD) and scanning electron microscopy (SEM) investigations allowed to determine the effect of deposition parameters on the thin films' microstructural changes. Changing the pulse width, while keeping the duty cycle constant, modified the discharge composition in the target region and the ionised fraction of the sputtered species in the substrate region. The maximum Cu ionised fraction (19 %) was found for 50 μs, resulting in compact and smooth morphology for Cu-rich films, whereas short 25 μs pulses provided porous columnar films with rough surfaces, as the result from Ar^+ bombardment. For Ag-rich films, Ag segregation allowed the deposition of dense layers, regardless of the used pulse width.

Furthermore, low Ag (<10 at.%) CuAgZr films produced via HiPIMS and direct-current magnetron sputtering (DCMS) were compared in terms of structural and mechanical property changes as a function of Zr contents. For the studied chemical composition range, a linear relationship between Zr content, XRD phase shift and mechanical properties was observed for HiPIMS films, in contrast to DCMS's more abrupt transitions. An increase in hardness and elastic modulus (up to 44 % and 22 %, respectively) was found for the HiPIMS films compared to DCMS ones. The obtained results highlight HiPIMS's flexibility in providing a wide range of tailoring possibilities to meet specific application requirements, such as crystalline microstructure, density and associated mechanical properties.

1. Introduction

The popularity of metallic glass (MG) has continuously increased since first studies began more than sixty years ago, as they are characterised by remarkable hardness (in the range of 3 to 5 GPa) and strength, while maintaining attractive physicochemical properties, such as corrosion resistance [1–6]. Such a combination of characteristics have led MGs to be of considerable interest for a range of applications, e.g. electronics, aeronautics, biomaterials, sports equipment, etc. [7,8]. MGs are generally produced via fast quenching of liquid into bulk form, after which the material is referred to as bulk metallic glass (BMG). There are certain limitations concerning BMG component dimensions, which is often imposed by the alloy's glass-forming ability (GFA), with maximum values reaching several centimetres [9]. Further casting method limitations include their relatively low cooling rates [10], where only narrow composition ranges, typically in the vicinity of deep eutectics characterised by high GFA [11], can be accessed. This significantly limits the range of attainable compositions of amorphous structures [10]. However, a possibility for overcoming these obstacles is depositing thin films of MGs (TFMGs) onto components via vapour deposition techniques [12]. TFMGs have recently emerged as alternative advanced surfaces for many applications, such as micro-electro-mechanical

* Corresponding author at: Feuerwerkerstrasse 39, 3603 Thun, Switzerland.
E-mail address: leo.lapeyre@empa.ch (L. Lapeyre).

https://doi.org/10.1016/j.surfcoat.2022.129002
Received 21 June 2022; Received in revised form 4 October 2022; Accepted 19 October 2022
Available online 24 October 2022

systems (MEMS) and for biomedical use, e.g. in the field of implants and surgical tools [8,13–15].

With a plethora of tuneable process parameters, thin film deposition techniques enable tailoring the properties of produced films, e.g. their chemical composition, atomic structure, or mechanical properties, in turn allowing for film optimisation for specific applications. The group of physical vapour deposition (PVD) methods provides the means to optimise the chemical composition of films and synthesise amorphous structures in a wider chemical composition range than conventional fast quenching methods [16]. Among those methods, high power impulse magnetron sputtering (HiPIMS) [17] exhibits the highest amount of adjustable process parameters. Where direct-current magnetron sputtering (DCMS) and radiofrequency (RF) process parameters are generally limited by the input average power, HiPIMS offers additional control parameters, such as pulse width, duty cycle, pulse frequency, or source synchronisation. These allow for the control of flux and energy of ions impinging the substrate surface and increased ad-atom mobility. In turn, this enables not only to optimise film chemical composition, but also to tune the film's density, surface roughness, structure, and mechanical properties [18–20]. Coupled with substrate biasing, the sputtered ion energy can be further managed, by providing an additional method to control which species reach the substrate region.

In this work, CuAgZr combinatorial material libraries were synthesised using state-of-the-art HiPIMS processes, as well as conventional DCMS. The CuAgZr system is of particular interest due to the possibility of obtaining films with high hardness and antimicrobial properties. Consequently, CuAgZr films are considered for surgical instrument [8] and dental applications [13], where besides high antimicrobial activity, high hardness (related to wear resistance) is a key property for the overall performance of the film [21]. Therefore, the main motivation of this work is to determine the possibility of tuning the composition, microstructure, and mechanical properties of films from the CuAgZr system using HiPIMS. Due to the complexity of the HiPIMS process, the first part of this work addresses the plasma species generated under different pulse width conditions (25, 50 and 100 μs) during Cu, Ag and Zr sputtering, while explaining the underlying HiPIMS physical phenomena [17]. To this end, optical emission spectroscopy (OES), modified quartz crystal microbalance (m-QCM) and time-of-flight mass spectrometry (TOFMS) were used to characterise the ionization region and the ion flux within the diffusion region, while following the discharge current evolution via HiPIMS I*(V,t)* curves. With changing plasma conditions, it is expected that the fabricated CuAgZr films microstructure, chemical composition and properties will also be affected, therefore ex situ film characterisation was performed. Finally, the properties of selected CuAgZr films produced via HiPIMS were compared with films of a similar chemical composition produced by means of DCMS.

2. Materials and methods

2.1. Deposition setup and film fabrication

A HexL modular deposition system (Korvus Technology, UK) was used as the vacuum chamber. The pumping setup was comprised of a primary dry scroll pump SH-110 (Agilent Technology, USA), and a turbomolecular pump HiPACE 700 (Pfeiffer Vacuum, Germany), enabling reaching a base pressure of 5×10^{-5} Pa. Three planar magnetrons (Korvus Technology, UK), equipped with SmCo magnets in unbalanced configuration (type II), were installed in the chamber at an angle of 27°, with respect to the *z*-axis of the chamber, with 120° between each source. Each magnetron was powered by 1 kW "Hipster 1" units (Ionautics, Sweden), which were, in turn, powered by programmable DC SL series power supplies (Magna-Power, USA). Each metallic target was installed on a separate magnetron, allowing to independently modify the sputtering conditions of each material, such as the pulse width and frequency. This enabled influencing the amount of deposited material and composition gradient. The rotating substrate holder, located 132 mm away from the sputtering sources, was connected to a DC power supply (TDK Lambda Corporation, Japan) for sample biasing. The chamber was additionally equipped with two electron cyclotron resonance (ECR) "Aura-wave" coaxial microwave (MW) sources (SAIREM, France) [22], with each source powered by a solid-state microwave generator at 2.45 GHz. More details on the chamber setup can be found in [23].

The HiPIMS CuAgZr films were deposited onto 4-inch p-type (100) silicon wafers (MicroChemicals, Germany) by sputtering from ∅ 50 mm, 3 mm thick targets (Kurt J. Lesker Company, USA) of copper (99.999 wt %), silver (99.99 wt%) and zirconium (grade 702, containing traces of hafnium). To facilitate film characterisation of different gradient zones, an in-house designed aluminium mask, with 61× ∅ 5 mm holes (10 mm spacing), was placed on top of the wafer (Fig. 1). Prior to deposition, the wafer was subjected to a pre-treatment process, which consisted of exposing it to a MW Ar plasma for 10 min at 0.2 Pa, to remove the native silicon oxide layer and any remaining contaminants. The MW sources were operated at 50 W each, with full substrate rotation (15 rpm) and biasing at −150 V to accelerate the Ar ions bombarding the wafer. In situ ellipsometry measurements confirmed the complete removal of native SiO_2 and the formation of an approx. 4 nm amorphous Si layer, due to Ar bombardment (results not included in this study). After pre-treatment, the bias voltage was reduced to −20 V, the Ar flow was set to 60 sccm, and the pressure was adjusted to 0.6 Pa (using an in-house fabricated butterfly valve). The microwave plasma was switched off just after the HiPIMS power supplies were turned on to inhibit substrate reoxidation. The sample holder was symmetrically rotated at an angle of 90° and at a speed of 10 rpm to reduce the chemical concentration spread of the deposited alloy. Each process was carried out at room temperature and lasted 8 h to reach film thicknesses of approx. 2 μm.

DCMS-produced samples were fabricated on 4-inch p-type Si (100) substrates coated with a protective 80 nm thick Si_3N_4 layer (MicroChemicals, Germany). The sputter targets (Kurt J. Lesker, UK) were high purity (99.99 %) 2-inch Cu, Ag, and Zr. For both HiPIMS and DCMS processes, the targets were pre-sputtered for 30 s to remove any surface contaminations. Co-sputtering of the three targets led to a composition gradient across the wafer. During deposition, the pressure in the chamber was maintained at 0.5 Pa, with an Ar (99.9999 % purity) flow of 60 sccm using standard mass flow controllers (MKS Instruments, USA). The sputtering power of the targets was optimised individually to achieve the desired composition gradient range. The sputtering parameters used for Cu, Ag, and Zr were 360 mA/85 V, 360 mA/28 V, and 345 mA/340 V, respectively. The deposition was carried out at room temperature for 5 h to achieve a film thickness in the range of 3 μm to facilitate further mechanical testing.

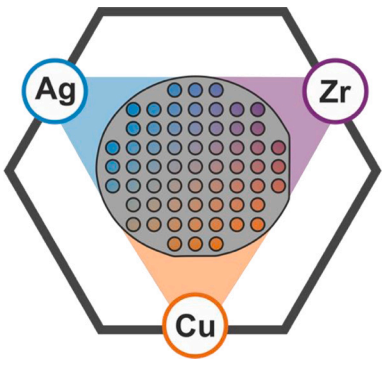

Fig. 1. Schematic of plasma source placement vs substrate and mask position;

2.2. In situ plasma diagnostics

OES was performed to obtain information on the atomic and ionic emission evolution during sputtering. To this end, three different spectrometers were used to investigate plasma emission. HR2000+ and HR2000 CG-UV-NIR (Ocean Optics, USA) detectors were used, with a spectral range of 200–480 nm and 190–1100 nm, respectively. For the observation of densely packed emission, a high-resolution 1 m focal length monochromator, with a 4800 g/mm grating in Cerny-Turner mount (Horiba, FR) was used. A 25 mm focal length f/2.8 quartz lens (Pentax, Japan) coupled with a QP400–2-SR-BX 200–1100 nm wavelength-ranged optical fibre (Ocean Optics, USA) were used to transmit the emitted light from the negative glow region of the magnetron to the spectrometer.

Ionised flux fraction measurements were performed using a ∅ 100 mm Quantum™ System m-QCM probe (Impedans Ltd., Ireland), to determine the mass deposition rate of neutral species and the total (neutral + ions) mass deposition rate. Measurements were performed in time-averaged mode at the height of the substrate. The ionic flux fraction was obtained through calculations described in the Results section.

The mass spectra were acquired using a prototype time-of-flight plasma sampling mass spectrometer (Tofwerk, Switzerland), providing mass spectra of all mass to charge ratios up to 500 Th with mass resolution (FWHM) of 500 for low mass to charge ratios (Ar^{2+}) and 1000 for heavier ions ($^{180}Hf^{+}$). The instrument includes an electrostatic energy analyser to measure plasma ion energies, however, the results reported here are all integrated over the full range of ion energies, assuming uniform transmission from the sampling interface as a function of energy. A 30 μm orifice positioned at the substrate height was used to sample ions from the plasma into the mass spectrometer (via differentially pumped transfer optics). During measurements, the orifice plate was at ground potential and the residual pressure in the sampling ion optics was below 5×10^{-3} Pa, therefore it is assumed that collisions after the sampling orifice that might lead to charge transfer or recombination reactions can be neglected.

The voltage and current output signals from the HiPSTER magnetron power supplies were monitored using a mixed signal oscilloscope (Tektronix, USA). Data were acquired using the averaging mode, based on 128 pulses.

2.3. Film characterisation

The chemical composition of the produced gradient films was analysed by means of X-ray fluorescence (XRF), using an X-ray XDV-SDD Fischerscope (Helmut Fischer AG, Germany). The beam energy was set to 50 kV and the spot size was 0.3 mm.

Structural analysis was performed via X-ray diffraction (XRD) using a Bruker D8 Discover diffractometer (Bruker, USA) with $CuK_{\alpha 1}$ and $CuK_{\alpha 2}$ radiations ($\lambda = 1.5406$ Å and 1.54439 Å, respectively). The $\theta/2\theta$ scans were performed in the range from 20 to 90°, with an offset of 2° from the symmetrical diffraction geometry (Bragg-Brentano configuration) to avoid the (400) reflection of the oriented (100) single crystal Si substrate. The measurement conditions were: 40 kV voltage, 40 mA current, step size of 0.02° and the collection time at each step was 2 s.

Surface morphology and fracture cross-sections were imaged using a Hitachi S-4800 high-resolution cold field emission (CFE) scanning electron microscope (SEM) (Hitachi High-Tech Corporation, Japan).

Nanoindentation was performed using a ZHN nanoindenter (Zwick Roell, Germany), equipped with a diamond Berkovich tip. The tip area function was calibrated for the selected measurement range prior to the measurements. Five measurements per patch were performed in load mode, the load was selected to not exceed a penetration depth of approx. 200 nm, i.e. ~10 % of film thickness. The elastic moduli were determined using the Oliver-Pharr method [24] using a Poisson's ratio of 0.37 [25].

3. Results

3.1. Plasma diagnostics

3.1.1. Ionization region

The investigated pulse widths were 25 μs, 50 μs and 100 μs and the HiPIMS processes were performed in constant voltage mode, using a fixed duty cycle to limit varying power effects. Pulse frequencies were adapted to target specific film chemical compositions, which will be described in greater detail in Section 3.2. The average power $\langle P \rangle$, average power per pulse P_{pulse} and energy per pulse E_{pulse} (Table 1) were calculated from HiPIMS I(*V,t*) curves of each target (Fig. 2). The $\langle P \rangle$ remained constant within 10 % for Ag and Zr, however, it doubled for Cu, due to significantly different temporal current evolution. The $\langle E_{pulse} \rangle$ followed the pulse width for Ag and Zr, and significantly increased for Cu by a factor of 8 between the 25 μs and 100 μs pulse widths. The Ag source reached a peak current of 6.5 A at 25 μs and then decreased to 4.2 A at a pulse width of 100 μs. A different behaviour was observed for Cu, where a peak current of 22 A was registered at a pulse width of approx. 40 μs, which remained stable for increased pulse durations of 50 μs and 100 μs. This corresponds to the increase in $\langle P_{pulse} \rangle$, when increasing the pulse width (Table 1). Using the Zr target the discharge current decreases by up to 50 %, when prolonging the pulse to 50 μs and 100 μs, respectively. The 50 μs pulse width has the highest average current, explaining the highest $\langle P_{pulse} \rangle$.

The emission spectra observed in the negative glow region of the magnetron discharges (see examples in Supplementary information) show a high density of recorded lines, making unambiguous line identification difficult. To address this difficulty, a "weighted mean emission intensity" approach was used to quantify the emission intensity, shown in Eqs. (1) and (2):

$$I_{mean} = \sum_{i=pixel} w(\lambda_i) \bullet I(\lambda_i) \tag{1}$$

$$w(\lambda_i) = \frac{I_{Nist}(\lambda_i)}{\sum_{i=pixel} I_{Nist}(\lambda_i)} \tag{2}$$

where $I(\lambda_i)$ is the measured intensity for the wavelength λ_i associated with the pixel I of the spectrometer detector, $w(\lambda_i)$ is a weighting factor based on the reported emission intensity I_{NIST}, following the NIST database.

As the pixel wavelength and the reported emission wavelength do not exactly coincide, the reported emission intensity was spread over the two adjacent pixel wavelengths according to the wavelength differences. Finally, to obtain the weight factors, the sum of all line intensities reported in the NIST data base [26] was normalised, for ease of interpretation. The weighted mean emission of the selected species (atomic and ionic argon and metals) is compared through weighted mean emission ratios and summarised in Table 2. The molecular emission lines observed in the Ag spectrum between 430 nm and 490 nm can be attributed to the $X^1\Sigma - A^1\Sigma$ transition of the Ag_2 dimer [27,28]. The Cu spectrum shows a high density of recorded lines in the range of 430–480 nm, where the strongest emission of the Cu_2 dimer is expected [29]. Doubly-ionised Cu and Zr ions were observed, while Ag was characterised by low ionic emissions and lack of Ag^{2+}.

3.1.2. Substrate region characterisation

Substrate region characterisation was performed via time-averaged m-QCM measurements to determine the influence of the pulse width on the ion flux reaching the substrate. The principle and description of the m-QCM can be found in [30]. Each deposition rate was measured for 200 s with an acquisition frequency of 1 Hz. The relative uncertainty of the absolute values of the deposition rates is estimated to be in the range of 50 %, while the uncertainty of the ionised flux fraction is approx. 10 %. The results of deposition rate measurements are displayed in Fig. 3.

Table 1
Discharge parameters during OES and I(*V,t*) curve measurements for Cu, Ag and Zr;

Target material	Pulse width [μs]	Frequency [Hz]	Duty cycle [%]	Voltage [V]	Peak Current [A]	Peak Current Density [A/cm^2]	⟨*P*⟩ [W]	⟨P_{pulse}⟩ [kW]	E_{pulse} [J]
Ag	25	100	0.25	900	6.5	0.32	11	4.42	0.11
	50	50					11	4.43	0.22
	100	25					11	4.35	0.43
Cu	25	300	0.75	800	18	0.89	44	7.3	0.18
	50	150			22	1.08	86	11.4	0.57
	100	1.0875					109	14.6	1.46
Zr	25	800	2	550	21	1.04	157	7.86	0.20
	50	400					185	9.28	0.46
	100	200					169	8.45	0.85

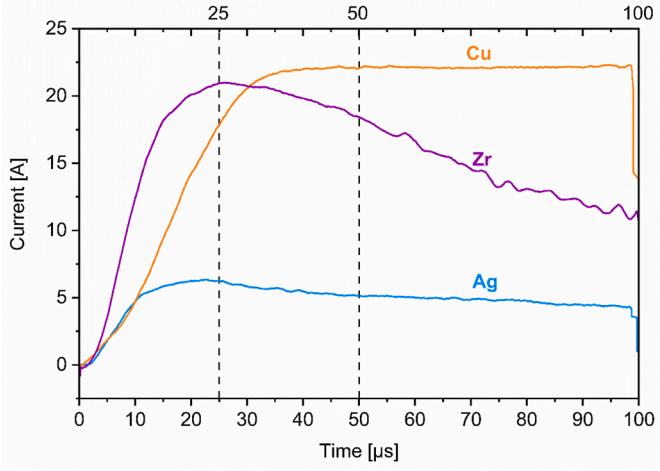

Fig. 2. Discharge current as a function of pulse width for Ag (blue), Cu (orange) and Zr (purple), pulse widths marked with vertical dashed lines (discharge parameters are given in Table 1); (For interpretation of the references to colour in this figure legend, the reader is referred to the web version of this article.)

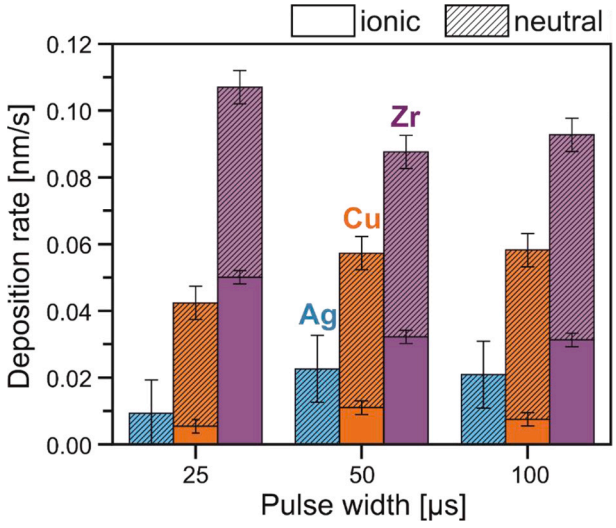

Fig. 3. Ag, Cu and Zr deposition rates, with distribution of neutral and ionic species, for 25, 50 and 100 μs pulse widths (detailed values given in *supplementary information*);

Table 2
Ratios of different weighted mean emission intensities observed for Ag, Cu and Zr for different pulse widths; No signal from M^{2+} on Ag source and Ar^+ on Zr source could be observed with certainty, explaining the missing values for the M^{2+}/M^+ and Ar^+/M^+ for these sources.

Target material	Pulse width [μs]	weighted mean emission intensity ratios			
		Ar/M	Ar^+/M^+	M^+/M	M^{2+}/M^+
Ag	25	0.27	0.26	0.31	–
	50	0.18	0.07	0.67	–
	100	0.14	0.13	0.51	–
Cu	25	0.45	0.61	0.11	0.30
	50	0.20	0.47	0.20	0.33
	100	0.12	0.50	0.24	0.34
Zr	25	0.27	–	0.52	0.05
	50	0.12	–	0.54	0.09
	100	0.11	–	0.53	0.07

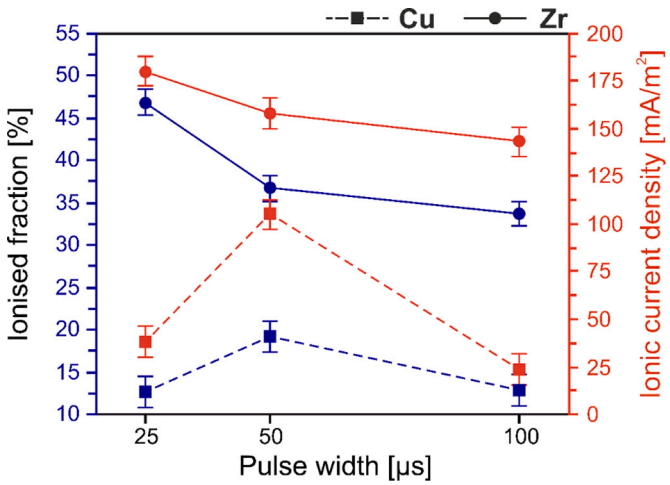

Fig. 4. Ionised fraction and ionic current density for Cu and Zr, with no ionic signal measured during Ag discharges (detailed values given in *supplementary information*);

The differences in the total deposition rates for the target materials are directly related to the pulse frequency of each source, as this directly influences the used average power. The drop experienced by Zr between 25 μs and 50 μs is related to a significant decrease in the ionic component. The increase in total deposition rate between shorter and longer pulses on Ag and Cu is due to the increase in the neutral component. The ionic current density shown in Fig. 4 is the highest for Zr, at 180 mA m^{-2} for 25 μs, and drops with increasing pulse width, in agreement with the ionised flux fraction. In the case of Cu, the ionic current density peaks at 110 mA m^{-2} for 50 μs (in line with the ionised fraction, Fig. 4) and is 4 times higher than for both shorter and longer pulses. This result is surprising, as the average power on Cu is 25 % higher for 100 μs compared to 50 μs. Moreover, OES showed an increased metallic ion generation at long pulses. For Cu and Zr, it can be summarised that the substrate experiences a neutral-dominated flux at long pulses, while 50 μs and 25 μs pulses provide the highest ionization. The Ag discharge provided a deposition rate of around 0.02 nm/s for each pulse width and no ionic component could be measured. Therefore, focus is kept on Cu and Zr.

In addition to the m-QCM measurements, the nature of the ions reaching the substrate area was determined using ToFMS and the results are summarised in Table 3. The extraction orifice was grounded, and applying a negative voltage did not strongly influence the relative contributions of the different ions. Given the mass resolving power of the mass analyser, ion identification was straight forward using the observed mass to charge ratio and further confirmed by the elemental isotopic pattern. For Ag, the ion flux is dominated by singly charged Ar ions, representing 60 % of the total flux, whereas for Cu and Zr the ion flux is dominated by singly charged metal ions. Singly charged metal dimer ions were detected for Ag and Cu, however, not for Zr. The proportion of doubly charged ions, for both argon and metals, is low. These ions do not seem to strongly contribute to the ion current at the substrate level.

3.2. CuAgZr film characterisation

3.2.1. HiPIMS-produced CuAgZr films

Three material libraries, with compositional gradients in the range of 43–73 at.% Cu, 11–37 at.% Ag and 13–48 at.% Zr, were fabricated via HiPIMS using three different pulse widths, i.e. 25 μs, 50 μs and 100 μs. These depositions were performed to determine the influence of pulse width on the films' structure, while targeting the border region for amorphous/crystalline phases within the CuAgZr system. Using the previously described mask, 61 patches were obtained on each wafer, of which 10 patches were selected for further analysis. Fig. 5 shows the chemical composition of the selected patches obtained via XRF from the centre of each patch (see Supplementary information for detailed chemical compositions). For a given alloy composition, the difference in chemical composition induced by the different pulse lengths is <3 at.%. From liquidus projections [11] of the CuAgZr system, reactive valleys (see grey lines in Fig. 5) are predicted to be present near the composition range of patches 3, 4, 5, 8, 9 and 10. Therefore, higher GFA is expected in these regions. A more pronounced crystallisation tendency is expected for patches 1, 2, 6, and 7.

Next, XRD was performed, with the diffractograms relevant for pulse width effect identification (patches 1, 3, 7, 8, 10) presented in Fig. 6 (see Supplementary information for remaining patches). As expected, crystalline structures were observed for patches far from the reactive zones. However, patch 3 (and 5), with a composition at the edge of the monotectic and peritectic regions, shows structural changes induced by changing the pulse width. Amorphous structures are obtained for 25 μs and 50 μs pulse widths, while 100 μs pulse widths provide crystallinity. On both patches, the dominant peak gradually shifts towards the Ag (111) phase, with increasing pulse duration. Another trend is observed on patch 7, characterised by the highest Cu content, where a considerable increase in crystallinity is observed for the 50 μs pulse width, with a significantly sharper Ag (111) peak compared to the 25 μs and 100 μs pulse widths. The amorphously structured patches (8 and 10) did not exhibit any specific trends on their respective x-ray diffractograms, in relation to the used pulse width.

The samples' surfaces and fracture cross-sections were analysed via SEM (Fig. 7). For all four selected patches, the roughest surfaces were attained under 25 μs pulse width conditions. The surfaces of the low Ag content patches (8 and 10) are defined by grains interrupted by a continuous network of pores, reflecting the inhomogeneous columnar growth seen on the film's fracture surface. In comparison, for the sample pulse width of 25 μs, the surface morphologies of high Ag content patches (1 and 3) are less porous and their fracture cross-sections are dense and non-columnar. A common trend is observed for Cu-rich patches (8 and 1), where the smoothest surfaces are found for 50 μs pulse widths, while a more granular morphology is observed using 100 μs. Films produced with both 50 and 100 μs pulse widths exhibit a dense and compact fracture cross-section and possess vein-like patterning,

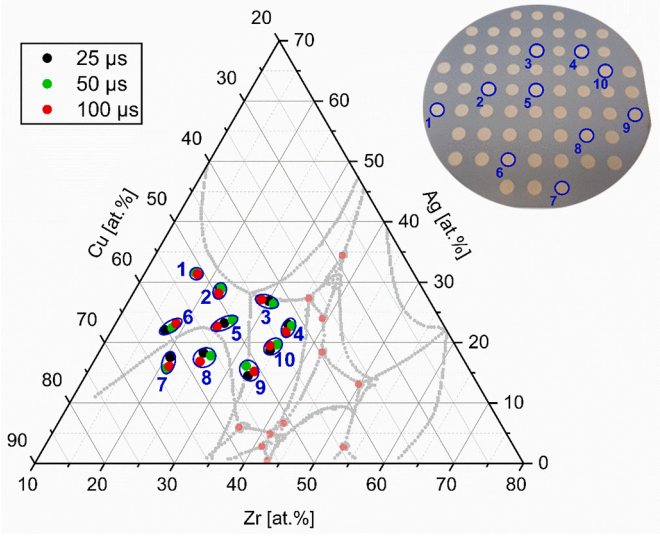

Fig. 5. CuAgZr ternary diagram, with points marking the compositions obtained using 25 (black), 50 (green), and 100 μs (red) pulse widths, blue circles indicate samples selected for XRD comparison, grey dotted lines highlight: M - monotectic, E - eutectic, P - peritectic points displayed from [11] using plot digitizer [46], insert shows a photograph of an example wafer with deposited patches; (For interpretation of the references to colour in this figure legend, the reader is referred to the web version of this article.)

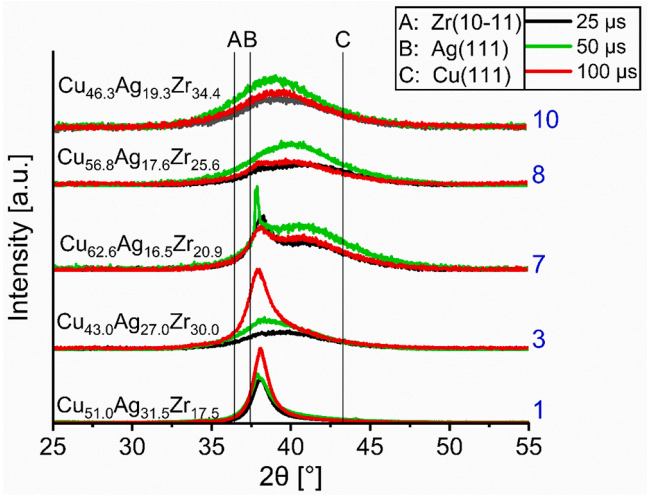

Fig. 6. X-ray diffractograms of patches 1, 3, 7, 8 and 10 fabricated using 25, 50 and 100 μs pulse widths, pure element diffraction peaks are observed for Zr (10−11) at $2\theta = 36.43°$, Ag (111) at $2\theta = 37.44°$ and Cu (111) at $2\theta = 43.275°$ (Cu, Ag and Zr reference lines taken from [47] at 0 K);

Table 3
Relative ion counts for Ag, Zr and Cu discharges, using 100 μs pulse widths and pulse conditions summarised in Table 1 (nominal isotopic masses supplied in bracket);

Target material	Ar^{++} / 20	Ar^{+} / 40	Ar_2^{+} / 80	M^{++}	M^{+}	M_2^{+}
Ag (107;109)	0.03	0.57	0.0009	0.001	0.4	0.0002
Zr (90;91;92;93;94;96)	0.025	0.36	0.006	0.025	0.58	0
Cu (63;65)	0.03	0.36	0.00015	0.000007	0.6	0.000005

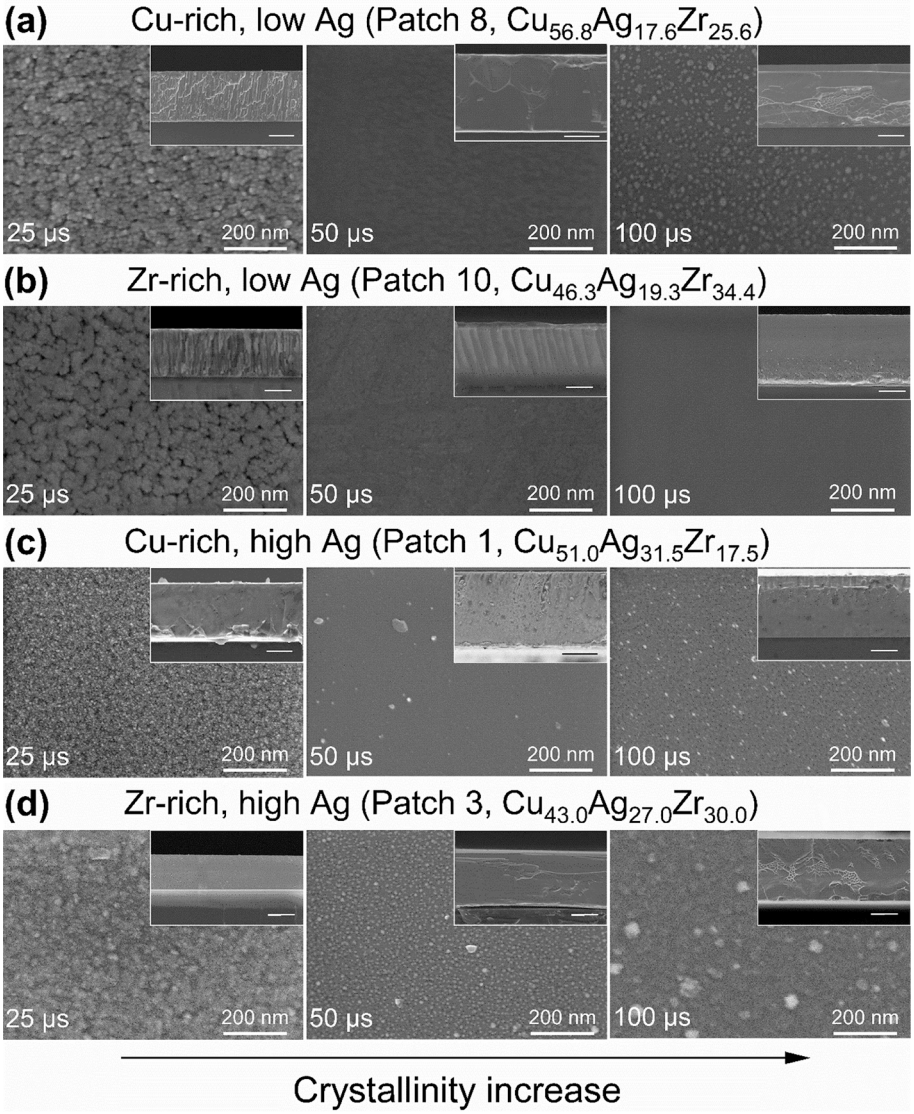

Fig. 7. Influence of 25, 50 and 100 µs pulse widths on the surface morphologies and fracture cross-sections of CuAgZr patches: 8 (a), 10 (b), 1 (c) and 3 (d), the scale bar on all fracture cross-section images represents 1 µm, SEM-SE;

characteristic of metallic glasses [31,32]. Furthermore, for Zr-rich patches (10 and 3), the surface becomes smoother when increasing the pulse width. The grain size of patch 3 seems to increase with increasing pulse widths, following the increasing crystallinity observed via XRD.

3.2.2. *HiPIMS- vs DCMS-produced low-Ag CuAgZr films*

The next stage of the study was to compare the structure and mechanical properties of HiPIMS- and DCMS-produced low-Ag content CuAgZr films. As was previously described plasma diagnostics and coatings characterisation, it was possible to establish that 50 µs pulse widths provide the highest ionization level for the Cu source, while facilitating the fabrication of highly dense and smooth films. This value was, therefore, used during the HiPIMS deposition of low-Ag sample. The magnetron settings of Cu, Ag and Zr sources were identical to the ones described in Table 1, except that the Ag frequency was reduced to 25 Hz to lower the Ag deposition rate. The DCMS parameters can be found in Section 2.1. To decorrelate the effect of pulse width and chemical composition on the microstructure of HiPIMS films, two samples (patches 2.1 and 2.8) of identical Ag content (4 at.%), but different Cu/Zr concentrations, were compared (Fig. 8). Patch 2.1 ($Cu_{70}Zr_{26}$), is highly dense and granular features can be found on its surface. Patch 2.8 ($Cu_{40}Zr_{56}$) is characterised by discontinuous columnar structuring, regardless of used pulse width. Similar results were observed when depositing pure Zr via HiPIMS [33]. The obtained patch compositions for both DCMS- and HiPIMS-fabricated films are presented in Fig. 9 (for details see Supplementary information). Four of the eight selected patches, with comparable Ag content (approx. 4 at.%), were selected for XRD (Fig. 10).

The HiPIMS films were predominantly amorphous. Two crystalline peaks, close to the (111) phase, were observed for patches 2.1 and 2.8 and could be related to the segregation Ag atoms in the structure. Furthermore, faint peaks near the Cu (111) phase can be seen. Compared to the reference lines, their right shift is most likely induced by tensile film stresses [34–36] (similarly to Fig. 6) and lattice strain of the solid solution, due to the presence of alloying elements with different atomic radii. The constant peak shift towards lower angles from patches 2.1 to 2.8 seems to follows the change in chemical composition towards higher Zr concentrations. The DCMS films are also mostly amorphous. The main reflections of patches 2.1 and 2.6 are sharper than their HiPIMS counterparts, and the shift towards lower angles is not linear. The asymmetry suggests chemical composition inhomogeneities in the films, namely the formation of Cu-rich regions in patch 2.1 ($Cu_{70}Ag_4Zr_{26}$) and Ag-rich regions in patches 2.6 ($Cu_{40}Ag_4Zr_{56}$) and 2.8 ($Cu_{40}Ag_4Zr_{56}$).

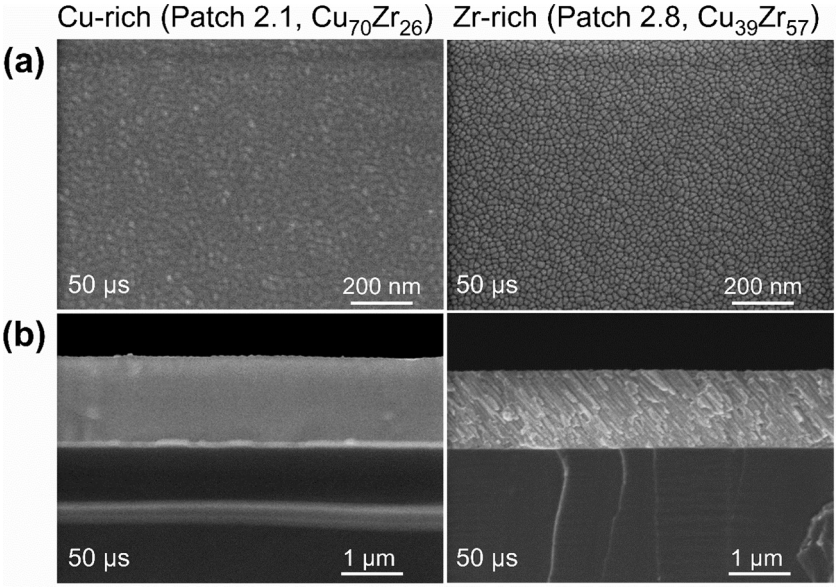

Fig. 8. Surface morphology (a) and fracture cross-section (b) of patches 2.1 ($Cu_{70}Ag_4Zr_{26}$) and 2.8 ($Cu_{40}Ag_4Zr_{56}$) deposited using 50 µs pulse widths, SEM-SE;

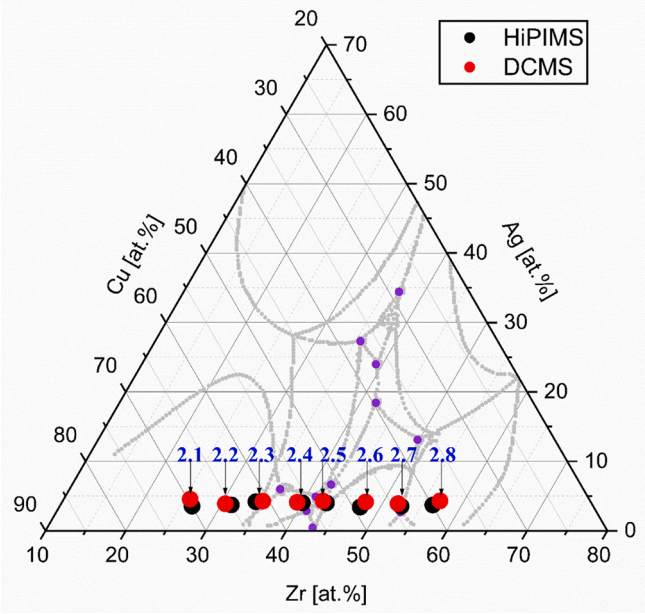

Fig. 9. CuAgZr ternary diagram, with marked compositions of low-Ag CuAgZr patches deposited via HiPIMS (black) and DCMS (red), selected compositions were analysed via XRD and nanoindentation; reaction zones highlighted using grey dotted lines and purple points show monotectic, eutectic and peritectic zones (refer to Fig. 6. for details); the numbering 2.# refers to the second series of produced samples, different from samples shown in Section 3.1; (For interpretation of the references to colour in this figure legend, the reader is referred to the web version of this article.)

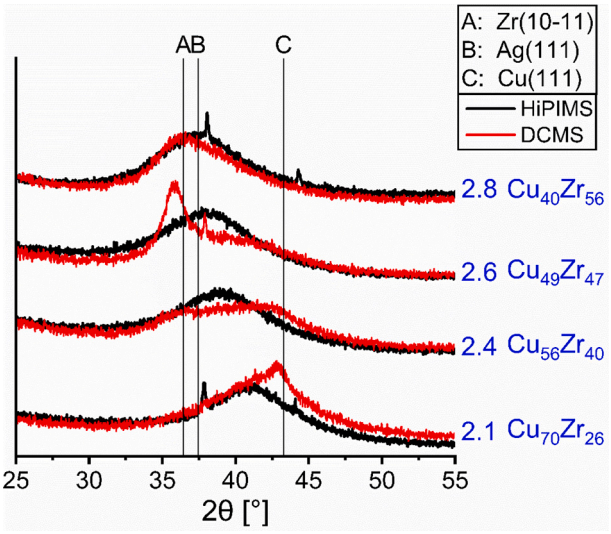

Fig. 10. XRD of patches 2.1, 2.4, 2.6, 2.8 produced via HiPIMS (black lines) and DCMS (red lines; pure element diffraction peaks are observed: Zr(0002) at $2\theta = 34.69°$, Zr(10–11) at $2\theta = 36.43°$, Ag (111) at $2\theta = 37.44°$ and Cu(111) at $2\theta = 43.275°$ (Cu, Ag and Zr reference lines taken from [47] at 0 K). the Ag content assumed to be constant for all patches (approx. 4 ± 0.3 at.%); (For interpretation of the references to colour in this figure legend, the reader is referred to the web version of this article.)

Considering that the films were synthesised in one process, i.e. under the same conditions, such observations suggest local variations in surface diffusion of the films' elements, depending on the area within the ternary system. This leads to the formation of regions enriched and depleted in alloy elements during the deposition process. An interesting observation is that despite clear evidence of surface diffusion, the structure of the resulting films remains amorphous or quasi-amorphous.

Next, nanoindentation was performed on all selected patches to determine their hardness and Young's modulus (Fig. 11). The results are plotted as a function of Zr content, with the Ag content assumed to be constant for all patches (approx. 4 ± 0.3 at.%). It should be noted that it was not possible to perform nanoindentation on patches 2.7 and 2.8 (highest Zr content), due to extensive porosity, which led to delamination during the measurements.

The mechanical properties are similar for HiPIMS and DCMS patches 2.1, 2.5 and 2.6, however, the overall trend differs. The HiPIMS patches are characterised by a linear decrease in hardness and elastic modulus with increasing Zr content, which reflects the porous and low density structures observed in Fig. 8a,b. The mechanical properties of the DCMS patches seem to be less correlated, with patches 2.2 and 2.3 showing a decrease in hardness and elastic modulus, followed by an increase for patches 2.4, 2.5 and 2.6. The greatest difference in mechanical properties between the DCMS and HiPIMS patches is observed for patches 2.2

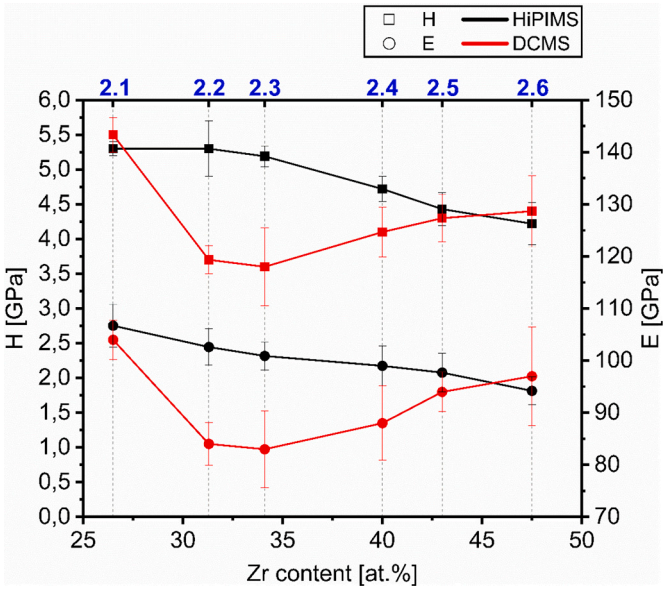

Fig. 11. Hardness (H) and elastic modulus (E) as a function of Zr content of HiPIMS- (black line) and DCMS- (red line) fabricated patches 2.1 to 2.6; (For interpretation of the references to colour in this figure legend, the reader is referred to the web version of this article.)

and 2.3, where the hardness increased by 44 % and elastic modulus by 22 % for the HiPIMS films. In an attempt to understand the reason behind the difference in mechanical properties of HiPIMS and DCMS patches 2.1 and 2.3, SEM was performed on the samples' fracture cross-sections (see Supplementary information). There are clear differences between the HiPIMS (dense, non-columnar) and DCMS (columnar) films, however, at this stage it was not possible to explain the differences in mechanical response.

4. Discussion

4.1. HiPIMS sputtering environment

In this work, pure Cu, Ag and Zr were used as sputtering targets. The differences in their deposition characteristics as a function of pulse width can be understood within the generalised recycling model, as presented by Brenning [37], and by referring to the fundamental properties of the studied materials (Supplementary information table S2). Starting with the discharge current evolution from Fig. 2, it can be seen that the Ag target is characterised by low currents regardless of used pulse width and voltage. This behaviour is a direct consequence of the high sputtering yield of Ag, which leads to a high silver atom density in the discharge region, which was confirmed by the detection of Ag_2 dimers by both OES and ToFMS (Table 3). Silver partly replaces Ar in the magnetron plasma, limiting the current rise [37], as singly charged Ag ions do not contribute to the generation of secondary electrons. Looking at the Zr discharge, a fast current rise reaching 21 A in 25 μs is facilitated by Zr's high secondary electron emission yield. As the sputtering yield of Zr in comparison to Ag is low, the partial replacement of Ar carrier gas atoms ions by sputtered Zr atoms requires significantly higher discharge currents. The relatively strong reduction in discharge current after passing the peak value can be explained by a combination of the low γ_{see} for Zr^{2+} ions and the low thermal conductivity of Zr, leading to target surface and carrier gas heating, enhancing the *gas rarefaction* phenomenon [38,39]. These trends are in line with m-QCM results, with the ionised fraction decreasing from 47 % at 25 μs to 34 % at 100 μs. The copper target reached a peak current of 22 A at 40 μs, which remained stable for longer pulse widths. The current rise is slow compared to Zr, due to low secondary electron emission yield (γ_{see} for Ag, Cu and Zr are 0.10, 0.08 and 0.13, respectively. See calculation method in Supplementary information) upon Ar^+ bombardment. The discharge current does not drop for longer pulses, due to the presence of doubly charged ions in the plasma, confirmed by both OES and ToFMS, and their strong contribution to the generation of secondary electrons. The copper discharge enters the *self-sputtering regime* [37,40–42]. The high ion density in the Cu discharge does not directly translate into and high ionised fraction for the 100 μs pulses due to the strong *back-attraction* phenomenon [40,43,44], which can be reduced by lowering the pulse widths to 50 μs, as confirmed by the m-QCM results. Following this assumption, one would expect the 25 μs pulse width to release the highest amount of ions. This holds true for Zr, where the peak current is reached within 25 μs. However, for Cu, the peak current is not reached until approx. 40 μs, therefore 25 μs pulse widths would provide a low ionised fraction regardless of the presence of ion back-attraction.

Summarising, Ag has a low ionic contribution to the deposition flux, regardless of the pulse width. The ionic flux is highest for 50 μs pulse widths for Cu and 25 μs pulse widths for Zr. Short pulses, i.e. 25 μs lead to an increased contribution of Ar^+ ions to the ionic flux.

4.2. HiPIMS plasma conditions vs CuAgZr film microstructure

The results obtained from plasma analysis can be related to the characteristics of the produced CuAgZr films, using the structure zone diagram (SZD) presented by A. Anders [45]. The relatively rough surface attained for short 25 μs pulse widths can possibly be related to the effect of Ar^+ ion bombardment, as these ions are dominant under such conditions. However, more detailed studies, including ion energy distribution function measurement would be needed to confirm this hypothesis. A significant difference in cross-section morphology is observed for the 25 μs patches with low (8 and 10) and high (1 and 3) Ag content, where high Ag content patches are characterised by dense and non-columnar structuring. This can be explained by the segregation of Ag species inside the pores and columns of the CuAgZr films, allowing for the growth of highly dense layers. This statement is supported by TEM measurements and elemental mapping of CuAgZr thin films, which will be presented in the following work (Huszar, private communication, 2022). Cu-rich films (patches 8 and 1) possess smoother surfaces when using 50 μs pulse widths, i.e. when the ion flux fraction for Cu is the highest (m-QCM results, Fig. 4). Additionally, high crystallinity was confirmed via XRD of patch 7 (62 at.% Cu), that was produced using 50 μs. The relatively high flux in ionised Cu has the effect of increasing the reduced temperature in the SZD. Zr-rich alloys obtain the smoothest surface for the longer, 100 μs pulses. For patch 3, this parameter also corresponds to a significant increase in crystallinity. Here, the effect of high ion flux on the reduced temperature is small, because of the low potential energy of Zr^+ ions, and the high melting point temperature of Zr. However, OES and ToFMS (not reported here in detail) results indicate that the metal to argon ratio is the highest for 100 μs pulses.

By referring to the SZD [45], the patches obtained under different pulse conditions can be classified. In the context of the produced CuAgZr films, those produced using 25 μs pulse widths containing low amounts of Ag (patches 8 and 10), can be attributed to the low energy region of *zone I*. These are characterised by fibrous columns, as well as by a porous and rough morphology. Patch 8, fabricated using 50 and 100 μs pulse widths (high Cu ionic flux) and characterised by high density and highly packed grains, resembles the characteristics of *zone T*. Patch 10, fabricated using 50 and 100 μs pulse widths, also possesses features resembling those of *zone T*. However, the 50 μs film could be further classified to the lower adatom mobility region of this zone regarding its dense but columnar structure, whereas the 100 μs film to the higher adatom mobility region of *zone T*, looking at the highly dense fracture surface. Furthermore, patches 1 and 3, containing high amounts of Ag and subjected to Ag segregation, can be attributed to *zone T* for all the studied pulse widths.

All obtained diffractograms were characterised by a right peak shift

with respect to the Ag (111) line, explained by the presence of solid solutions, with possible contribution from tensile stresses, as already observed for CuZr alloys [34–36]. The broadening and asymmetry of peaks observed on textured patches are associated with the presence of chemical gradients, causing crystal lattice strain. This effect hindered result interpretation, however, it can be stated that HiPIMS pulse widths strongly influence the microstructure of crystalline zones of the CuAgZr system.

Finally, when comparing the films obtained via DCMS and HiPIMS, the latter is not only more effective in metallic glasses synthesis, but also offers a wider selection of film properties, as observed with the constant shift of the diffractograms with changing Zr composition at a given pulse width (Fig. 10). This is additionally confirmed by mechanical properties measurements (Fig. 11), as a linear decrease in hardness and elastic modulus with increasing Zr content was observed.

5. Conclusions

This work focused on characterising the deposition environment during HiPIMS Cu, Ag and Zr discharges under various pulse width conditions, as well as determining its effect on the properties of CuAgZr films. The combination of different plasma diagnostic tools (OES, ToFMS and m-QCM) was used to obtain a complete picture of the deposition environment for each target material, in relation to the physical phenomena occurring during HiPIMS discharges. It can be concluded that the 50 μs pulse width provides the best compromise for all investigated target materials, as it allows to lower gas rarefaction and ion back-attraction effects, while providing enough time to initiate metallic ion production on each source.

The different pulse width conditions strongly influenced the microstructure, as observed via SEM and XRD. Cu-rich films showed smoother and denser microstructures (*zone T*). when using 50 μs pulse widths. This corresponds to the highest ionised fraction and ionic current density on the Cu source. Under this condition, the highest Cu content film (patch 7) experienced a significant increase in crystallinity. Short 25 μs pulses induce rough surfaces, most likely due to strong Ar bombardment. Short pulses also provided porous and columnar-structured (*zone I*) films, when the Ag content remains under 20 at.%. At high Ag concentrations (approx. 30 at.%), the films were characterised by dense and non-columnar films, regardless of the pulse width. This is most probably due to the segregation of Ag atoms in the CuAgZr layer. Films fabricated using 100 μs pulse widths were found to be dense for every patch composition, and tended to provide crystalline structures, depending on the alloy composition. The reduction in Ar species at longer pulses is in line with the obtained results.

By comparing the structure and mechanical properties of HiPIMS- and DCMS-fabricated films of comparable chemical compositions, it was shown that HiPIMS provides more control over the produced thin film properties as a function of chemical composition. Additionally, improved mechanical properties were obtained when using HiPIMS over DCMS, with hardness and elastic modulus increases of up to 44 % and 22 %, respectively, for film composition between $Cu_{66}Ag_4Zr_{30}$ and $Cu_{56}Ag_4Zr_{40}$.

The findings of this work provide important information to better understand the evolution of the complex plasma phenomena occurring during HiPIMS when changing the used pulse width. This, in turn, facilitates sputtering process optimisation of materials of similar compositions to those investigated in this study. Moreover, the results showing the microstructural dependence on the pulse width, as well as improvement in mechanical properties of the films from the CuAgZr system compared to DCMS highlight the versatility of HiPIMS and its tremendous potential for MG applications.

CRediT authorship contribution statement

L. Lapeyre: depositions, investigations and analysis, preparing original draft; *K. Wieczerzak*: conceptualisation, supervision, investigations and analysis, draft revision and editing; *C. Hain*: investigations and analysis, draft revision and editing; *J. Metzger:* mass spectrometric measurements and analysis, draft revision and editing; *A. Sharma*: depositions, draft revision and editing; *A. Bensaoula*: supervision, draft revision and editing, *J. Michler*: supervision, resources, draft revision and editing; *T. Nelis*: conceptualisation, supervision, resources, draft revision and editing.

Declaration of competing interest

The authors declare that they have no known competing financial interests or personal relationships that could have appeared to influence the work reported in this paper.

Data availability

Data will be made available on request.

Acknowledgements

This work was co-funded by the Innosuisse-Swiss Innovation Agency and the European Union as part of project E!114277 IonDrive. K.W. acknowledges the EMPAPOSTDOCS-II programme that has received funding from the European Union's Horizon 2020 research programme under the Marie Skłodowska-Curie grant agreement number 754364.

Appendix A. Supplementary data

Supplementary data to this article can be found online at https://doi.org/10.1016/j.surfcoat.2022.129002.

References

[1] M.M. Trexler, N.N. Thadhani, Mechanical properties of bulk metallic glasses, Prog. Mater. Sci. 55 (2010) 759–839, https://doi.org/10.1016/J.PMATSCI.2010.04.002.
[2] H.W. Chen, K.C. Hsu, Y.C. Chan, J.G. Duh, J.W. Lee, J.S.C. Jang, G.J. Chen, Antimicrobial properties of zr-cu-Al-ag thin film metallic glass, Thin Solid Films 561 (2014) 98–101, https://doi.org/10.1016/J.TSF.2013.08.028.
[3] P. Du, T. Xiang, X. Yang, G. Xie, Enhanced mechanical and antibacterial properties of cu-bearing ti-based bulk metallic glass by controlling porous structure, J. Alloys Compd. 904 (2022), https://doi.org/10.1016/J.JALLCOM.2022.164005.
[4] V.M. Villapún, S. Tardío, P. Cumpson, J.G. Burgess, L.G. Dover, S. González, Antimicrobial properties of cu-based bulk metallic glass composites after surface modification, Surf. Coat. Technol. 372 (2019) 111–120, https://doi.org/10.1016/J.SURFCOAT.2019.05.041.
[5] A. Sagasti, A.C. Lopes, A. Lasheras, Corrosion resistant metallic glasses for biosensing applications COLLECTIONS, AIP Adv. 8 (2018) 47702, https://doi.org/10.1063/1.4994108.
[6] J. Schroers, G. Kumar, T.M. Hodges, S. Chan, T.R. Kyriakides, Bulk metallic glasses for biomedical applications, JOM 61 (9) (2009) 61, https://doi.org/10.1007/S11837-009-0128-1 (2009) 21–29.
[7] S.H. Chen, H.Y. Cheng, K.C. Chan, G. Wang, Metallic Glass Structures for Mechanical-Energy-Dissipation Purpose: A Review, Metals 8 (2018) 689, https://doi.org/10.3390/MET8090689, 8 (2018) 689.
[8] S.T. Rajan, A. Arockiarajan, Thin film metallic glasses for bioimplants and surgical tools: a review, J. Alloys Compd. 876 (2021), https://doi.org/10.1016/J.JALLCOM.2021.159939.
[9] G. Kumar, A. Desai, J. Schroers, Bulk metallic glass: the smaller the better, Adv. Mater. 23 (2011) 461–476, https://doi.org/10.1002/ADMA.201002148.
[10] T. Kozieł, K. Pajor, Ł. Gondek, Cooling rate evaluation during solidification in the suction casting process, Journal of Materials Research and Technology. 9 (2020) 13502–13508, https://doi.org/10.1016/J.JMRT.2020.09.082.
[11] D.H. Kang, I.H. Jung, Critical thermodynamic evaluation and optimization of the Ag–Zr, Cu–Zr and Ag–Cu–Zr systems and its applications to amorphous Cu–Zr–Ag alloys, Intermetallics (Barking). 18 (2010) 815–833, https://doi.org/10.1016/J.INTERMET.2009.12.013.
[12] D. Turnbull, Metastable structures in metallurgy, Metallurgical Transactions B 12 (2) (1981) 12, https://doi.org/10.1007/BF02654454 (1981) 217–230.
[13] C.N. Cai, C. Zhang, Y.S. Sun, H.H. Huang, C. Yang, L. Liu, ZrCuFeAlAg thin film metallic glass for potential dental applications, Intermetallics (Barking). 86 (2017) 80–87, https://doi.org/10.1016/J.INTERMET.2017.03.016.
[14] P.H. Tsai, Y.Z. Lin, J.B. Li, S.R. Jian, J.S.C. Jang, C. Li, J.P. Chu, J.C. Huang, Sharpness improvement of surgical blade by means of ZrCuAlAgSi metallic glass and metallic glass thin film coating, Intermetallics (Barking). 31 (2012) 127–131, https://doi.org/10.1016/J.INTERMET.2012.06.014.

[15] J.S.C. Jang, P.H. Tsai, A.Z. Shiao, T.H. Li, C.Y. Chen, J.P. Chu, J.G. Duh, M.J. Chen, S.H. Chang, W.C. Huang, Enhanced cutting durability of surgical blade by coating with fe-based metallic glass thin film, Intermetallics (Barking). 65 (2015) 56–60, https://doi.org/10.1016/J.INTERMET.2015.06.012.
[16] G.B. Bokas, L. Zhao, D. Morgan, I. Szlufarska, Increased stability of CuZrAl metallic glasses prepared by physical vapor deposition, J. Alloys Compd. 728 (2017) 1110–1115, https://doi.org/10.1016/J.JALLCOM.2017.09.068.
[17] D. Lundin, J.T. Gudmundsson, T. Minea, High power impulse magnetron sputtering : fundamentals, technologies, challenges and applications, Elsevier (2019), https://doi.org/10.1016/C2016-0-02463-4.
[18] T. Shimizu, H. Komiya, T. Watanabe, Y. Teranishi, H. Nagasaka, K. Morikawa, M. Yang, HIPIMS deposition of TiAlN films on inner wall of micro-dies and its applicability in micro-sheet metal forming, Surf. Coat. Technol. 250 (2014) 44–51, https://doi.org/10.1016/j.surfcoat.2014.02.008.
[19] M. Samuelsson, D. Lundin, J. Jensen, M.A. Raadu, J.T. Gudmundsson, U. Helmersson, On the film density using high power impulse magnetron sputtering, Surf. Coat. Technol. 205 (2010) 591–596, https://doi.org/10.1016/J.SURFCOAT.2010.07.041.
[20] J. Paulitsch, P.H. Mayrhofer, W.D. Münz, M. Schenkel, Structure and mechanical properties of CrN/TiN multilayer coatings prepared by a combined HIPIMS/UBMS deposition technique, Thin Solid Films 517 (2008) 1239–1244, https://doi.org/10.1016/j.tsf.2008.06.080.
[21] C.Y. Chuang, J.W. Lee, C.L. Li, J.P. Chu, Mechanical properties study of a magnetron-sputtered zr-based thin film metallic glass, Surf. Coat. Technol. 215 (2013) 312–321, https://doi.org/10.1016/J.SURFCOAT.2012.04.101.
[22] L. Latrasse, M. Radoiu, T. Nelis, O. Antonin, Self-matching plasma sources using 2.45 GHz solid-state generators: microwave design and operating performance, J. Microw. Power Electromagn. Energy. 51 (2017) 237–258, https://doi.org/10.1080/08327823.2017.1388338.
[23] C. Hain, D. Brown, A. Welsh, K. Wieczerzak, R. Weiss, J. Michler, A. Hessler-Wyser, T. Nelis, From pulsed-DCMS and HiPIMS to microwave plasma-assisted sputtering: Their influence on the properties of diamond-like carbon films, Surf Coat Technol. (2021) 127928, https://doi.org/10.1016/j.surfcoat.2021.127928.
[24] G.M. Pharr, W.C. Oliver, Measurement of thin film mechanical properties using nanoindentation, MRS Bull. (1992), https://doi.org/10.1557/S0883769400041634.
[25] G. Duan, K. de Blauwe, M.L. Lind, J.P. Schramm, W.L. Johnson, Compositional dependence of thermal, elastic, and mechanical properties in cu-zr-ag bulk metallic glasses, Scr. Mater. 58 (2008) 159–162, https://doi.org/10.1016/j.scriptamat.2007.10.001.
[26] Y. Ralchenko, A. Kramida, Development of NIST atomic databases and online tools, Atoms. 8 (2020), https://doi.org/10.3390/ATOMS8030056.
[27] R.R. Laher, M.A. Khakoo, A. Antić-Jovanović, Radiative transition parameters for the a 1 Σu+ - X 1 Σg+ band system of 107,109Ag2, J. Mol. Spectrosc. 248 (2008) 111–121, https://doi.org/10.1016/j.jms.2007.12.003.
[28] B. Kleman, S. Lindkvist, The band-Spectrum of the Ag2-molecule, Arkiv För Fysik. 9 (1955) 385–390.
[29] B. Kleman, S. Lindkvist, The band-Spectrum of the Cu2-molecule, Arkiv För Fysik. 8 (1954) 333–339.
[30] S. Sharma, D. Gahan, P. Scullin, J. Doyle, J. Lennon, R.K. Vijayaraghavan, S. Daniels, M.B. Hopkins, Measurement of deposition rate and ion energy distribution in a pulsed dc magnetron sputtering system using a retarding field analyzer with embedded quartz crystal microbalance, Rev. Sci. Instrum. 87 (2016), https://doi.org/10.1063/1.4946788.
[31] B.A. Sun, W.H. Wang, The fracture of bulk metallic glasses, Prog. Mater. Sci. 74 (2015) 211–307, https://doi.org/10.1016/j.pmatsci.2015.05.002.
[32] S. Comby-Dassonneville, T. Venot, A. Borroto, E. Longin, C. der Loughian, B. ter Ovanessian, M.A. Leroy, J.F. Pierson, P. Steyer, ZrCuAg thin-film metallic glasses: toward biostatic durable advanced surfaces, ACS Appl. Mater. Interfaces 13 (2021) 17062–17074, https://doi.org/10.1021/acsami.1c01127.
[33] C.C. Kuo, C.H. Lin, J.T. Chang, Y.T. Lin, Effect of voltage pulse width and synchronized substrate bias in high-power impulse magnetron sputtering of zirconium films, Coatings. 11 (2021) 1–13, https://doi.org/10.3390/coatings11010007.
[34] J. Chakraborty, T. Oellers, R. Raghavan, A. Ludwig, G. Dehm, Microstructure and residual stress evolution in nanocrystalline cu-zr thin films, J. Alloys Compd. 896 (2022), 162799, https://doi.org/10.1016/J.JALLCOM.2021.162799.
[35] P. Zeman, M. Zítek, Zuzjaková, R, Čerstvý, Amorphous Zr-Cu thin-film alloys with metallic glass behavior, J Alloys Compd. 696 (2017) 1298–1306, https://doi.org/10.1016/J.JALLCOM.2016.12.098.
[36] T. Oellers, R. Raghavan, J. Chakraborty, C. Kirchlechner, A. Kostka, C.H. Liebscher, G. Dehm, A. Ludwig, Microstructure and mechanical properties in the thin film system cu-zr, Thin Solid Films 645 (2018) 193–202, https://doi.org/10.1016/J.TSF.2017.10.030.
[37] N. Brenning, J.T. Gudmundsson, M.A. Raadu, T.J. Petty, T. Minea, D. Lundin, A unified treatment of self-sputtering, process gas recycling, and runaway for high power impulse sputtering magnetrons, Plasma Sources Sci. Technol. 26 (2017), https://doi.org/10.1088/1361-6595/aa959b.
[38] C. Huo, M.A. Raadu, D. Lundin, J.T. Gudmundsson, A. Anders, N. Brenning, Gas rarefaction and the time evolution of long high-power impulse magnetron sputtering pulses, Plasma Sources Sci. Technol. 21 (2012), https://doi.org/10.1088/0963-0252/21/4/045004.
[39] T. Kozák, J. Lazar, Gas rarefaction in high power impulse magnetron sputtering: comparison of a particle simulation and volume-averaged models, Plasma Sources Sci. Technol. 27 (2018), https://doi.org/10.1088/1361-6595/aaebdd.
[40] A. Anders, J. Andersson, A. Ehiasarian, High power impulse magnetron sputtering: current-voltage-time characteristics indicate the onset of sustained self-sputtering, J. Appl. Phys. 102 (2007), https://doi.org/10.1063/1.2817812.
[41] A. Anders, Self-sputtering runaway in high power impulse magnetron sputtering: the role of secondary electrons and multiply charged metal ions, Appl. Phys. Lett. (2008), https://doi.org/10.1063/1.2936307.
[42] C. Huo, D. Lundin, M.A. Raadu, A. Anders, J.T. Gudmundsson, N. Brenning, On the road to self-sputtering in high power impulse magnetron sputtering: particle balance and discharge characteristics, Plasma Sources Sci. Technol. 23 (2014), https://doi.org/10.1088/0963-0252/23/2/025017.
[43] T. Shimizu, M. Zanáška, R.P. Villoan, N. Brenning, U. Helmersson, D. Lundin, Experimental verification of deposition rate increase, with maintained high ionized flux fraction, by shortening the HiPIMS pulse, Plasma Sources Sci. Technol. 30 (2021), https://doi.org/10.1088/1361-6595/abec27.
[44] V. Tiron, I.L. Velicu, I. Mihăilă, G. Popa, Deposition rate enhancement in HiPIMS through the control of magnetic field and pulse configuration, Surf. Coat. Technol. 337 (2018) 484–491, https://doi.org/10.1016/J.SURFCOAT.2018.01.065.
[45] A. Anders, A structure zone diagram including plasma-based deposition and ion etching, Thin Solid Films 518 (2010) 4087–4090, https://doi.org/10.1016/j.tsf.2009.10.145.
[46] Ankit Rohatgi, WebPlotDigitizer, Https://Automeris. Io/WebPlotDigitizer. (2021).
[47] A. Jain, S.P. Ong, G. Hautier, W. Chen, W.D. Richards, S. Dacek, S. Cholia, D. Gunter, D. Skinner, G. Ceder, K.A. Persson, Commentary: the materials project: a materials genome approach to accelerating materials innovation, APL Mater. 1 (2013), 011002, https://doi.org/10.1063/1.4812323.